Structural response of concrete-filled elliptical steel hollow sections under eccentric compression

T. Sheehan[a], X. H. Dai[b], T.M. Chan[a*], D. Lam[b]

[a]*School of Engineering, University of Warwick, Coventry CV4 7AL, United Kingdom*

[b]*School of Engineering, Design &Technology, University of Bradford, Bradford BD7 1DP, United Kingdom*

*corresponding author: t.m.chan@warwick.ac.uk; tel: +44 (0)24 76522106; fax: +44 (0)24 76418922

Abstract

The purpose of this research is to examine the behaviour of elliptical concrete-filled steel tubular stub columns under a combination of axial force and bending moment. Most of the research carried out to date involving concrete-filled steel sections has focussed on circular and rectangular tubes, with each shape exhibiting distinct behaviour. The degree of concrete confinement provided by the hollow section wall has been studied under pure compression but remains ambiguous for combined compressive and bending loads, with no current design provision for this loading combination. To explore the structural behaviour, laboratory tests were carried out using eight stub columns of two different tube wall thicknesses and applying axial compression under various eccentricities. Moment-rotation relationships were produced for each specimen to establish the influence of cross-section dimension and axis of bending on overall response. Full 3D finite element models were developed, comparing the effect of different material constitutive models, until good agreement was found. Finally, analytical interaction curves were generated assuming plastic behaviour and compared with the experimental and finite element results. Ground work provided from these tests paves the way for the development of future design guidelines on the member level.

Keywords

Concrete-filled tubes; Elliptical hollow sections; Eccentric compression; Numerical modelling; Experimental analysis; Interaction curves.

Notations

a = major (maximum) radius of ellipse

A_c = area of concrete in cross-section

A_{cc} = area of concrete in compression

a_m = major (maximum) radius (from centre of ellipse to mid-thickness of tube)

A_s = area of steel section

A_{sc} = area of steel in compression

A_{st} = area of steel in tension

b = minor (minimum) radius of ellipse

b_m = minor (minimum) radius (from centre of ellipse to mid-thickness of tube)

D_e = equivalent circular diameter for ellipse

$D_{e,c}$ = equivalent diameter for section in compression

$D_{e,b}$ = equivalent diameter for section in bending

e = loading eccentricity

e' = loading eccentricity normalised with respect to cross-section depth

E_{cc} = static elastic modulus of confined concrete

f = function for determining D_e (equation (4))

f = concrete stress in constitutive relationship (equation (11), [17])

f_{cc} = compressive strength of confined concrete

f_{ck} = compressive strength of unconfined concrete

f_e = confined concrete stress at point of transition between softening regions

f_l = concrete strength enhancement value (equation (10))

f_u = ultimate stress of confined concrete

f_y = yield stress of steel

k_1 = coefficient for determining f_{cc}

k_2 = coefficient for determining ε_{cc}

k_3 = coefficient for ultimate concrete stress

M = bending moment

M_{FE} = moment corresponding to maximum load (FE)

M_{hollow} = bending moment corresponding to maximum load for hollow specimens [5]

M_{test} = moment corresponding to maximum load (experiment)

N = axial force

N_{hollow} = maximum axial load for hollow specimens [5]

$N_{max,FE}$ = maximum axial load from finite element analysis

$N_{max,test}$ = maximum axial load from experiments

R_c = distance between centre of ellipse and steel-concrete interface

R_E , R_σ, R_ε = parameters for stress-strain relationship of confined concrete [17]

t = tube wall thickness

W_{pl} = plastic modulus of steel section

$W_{pl,cc}$ = plastic modulus of concrete in compression

$W_{pl,sc}$ = plastic modulus of steel in compression

$W_{pl,st}$ = plastic modulus of steel in tension

x = normalised concrete strain

y = normalised concrete stress

α, β = angles defining position of point on ellipse perimeter

β_0, η = parameter for stress-strain relationship of confined concrete [18]

ε = coefficient depending on f_y [15]

ε = concrete strain in constitutive relationship (equation (11), [17])

ε_{cc} = strain corresponding to maximum compressive stress of confined concrete

ε_{ck} = strain corresponding to maximum compressive stress of unconfined concrete

ε_e = confined concrete strain at point of transition between softening regions

ε_u = ultimate strain of confined concrete

ξ = ratio of steel to concrete in cross-section axial resistance

σ_0 = compressive strength of concrete

ψ = ratio of cross-sectional stresses at extreme fibres

1. Introduction

Concrete-filled tubes are highly suitable for use as column members in structures, owing to their superior strength, constructability and appearance in comparison with numerous other types of cross-section. In this efficient arrangement, the outer steel tube prevents or delays lateral expansion and failure of the concrete core, which in turn mitigates inward buckling of the steel hollow section. This behaviour is influenced by the tube shape, as discussed by Susantha et al. [1], with the optimum strength achieved by circular sections. The non-uniformity of the perimeter in square and rectangular tubes both increases the susceptibility to local buckling and leads to a variation in confining pressure to the concrete core, resulting in inferior resistance to that of a circular section. To date, a considerable degree of research has been executed on square, rectangular and circular sections, leading to design guidelines such as EN1994-1-1 [2].

The use of elliptical tubes is increasingly popular, owing to the presence of both major and minor axes, which potentially improve the efficiency and aesthetics of the member in certain applications. Hollow elliptical sections have been tested under compression by Chan and Gardner [3], bending by Chan and Gardner [4], and combined compression and bending by Gardner et al. [5], leading to a number of design recommendations. The cross-sectional buckling behaviour of hollow elliptical sections has been found to lie between that of a circular tube and a flat plate, as demonstrated by Chan and Gardner [3], Ruiz-Teran and Gardner [6]. Tests have also been conducted applying pure compression to concrete-filled

elliptical stub columns, such as Yang et al. [7] and Zhao and Packer [8]. The strength of these sections was found to be inferior to equivalent circular sections, owing to the varying curvature of the steel perimeter and non-uniform confining pressure to the concrete core. Further to these tests, a considerable degree of finite element modelling has been carried out for concrete-filled tubes, owing to the speed and economy offered in comparison with conducting laboratory experiments. Full 3D finite element models were created by Dai and Lam [9-10], for elliptical concrete-filled tubes under pure compression. Here, an existing constitutive model for concrete confined by circular tubes by Hu and Schnobrich [11] and Hu et al. [12] was modified for application to elliptical sections and satisfactory agreement was achieved with experimental results.

Following from the research of [7]-[10] there is now scope to assess the performance of concrete-filled elliptical stub columns under eccentric compression. Interaction curves have already been developed for circular and rectangular sections under combined bending and compression in EN1994-1-1 [2] and CIDECT [13] but there is no equivalent guidance for elliptical cross-sections. The difference between the maximum and minimum curvatures provides varying confinement to different regions of the concrete and possibly differing behaviour between each axis of bending. Hence a series of experiments was conducted, applying combined compression and bending to elliptical cross-sections, comparing different tube wall thicknesses for both major and minor axis bending. Following this, finite element models were developed to assess the suitability of previously developed confined concrete models for this loading application, to enable further parametric studies.

2. Experimental program

A series of tensile steel material tests, compressive concrete material tests and stub column tests under eccentric compression were carried out to investigate the structural response of

concrete-filled elliptical steel hollow sections under eccentric compression. All tests were performed in the Structures Laboratory of the School of Engineering, University of Warwick.

2.1 Specimen geometry

Eccentric compression was applied to eight concrete-filled elliptical stub columns. All specimens were 300 mm long, with cross-section dimensions of 150 × 75 mm (2a × 2b as shown in Fig. 1). This gave an aspect ratio of 2 for the cross-section, to facilitate comparisons with results from previous researchers, such as Yang et al. [7].

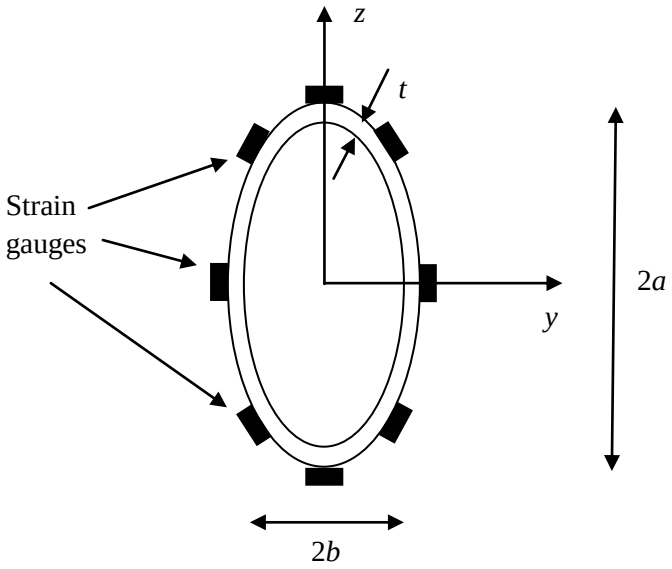

Fig. 1. Specimen dimensions and strain gauge locations

Prior to conducting the experiments, the actual tube wall thickness was measured at a number of locations around the perimeter of each section and local imperfections were also measured by recording the surface profile at 20 mm intervals along each of the specimen faces. The specimen identifications, average measured wall thickness, applied loading and maximum measured imperfections are summarised in Table 1. The first part of the specimen ID refers to the axis of bending followed by the nominal loading eccentricity in mm, in which 'MA'

denotes bending about the major axis and 'MI' denotes bending about the minor axis. The second part of the ID indicates the nominal tube wall thickness, also given in mm.

Table 1. Test Specimen Details.

Specimen ID	Average measured wall thickness	Bending axis	Load eccentricity	Max imperfection
	(mm)		(mm)	(mm)
MA100-6.3	6.67	Major (y-y)	100	0.16
MA25-6.3	6.63	Major (y-y)	25	0.06
MI75-6.3	6.62	Minor (z-z)	75	0.06
MI25-6.3	6.58	Minor (z-z)	25	0.07
MA100-5	4.76	Major (y-y)	100	0.05
MA25-5	4.83	Major (y-y)	25	0.05
MI75-5	4.91	Minor (z-z)	75	0.45
MI25-5	4.88	Minor (z-z)	25	0.17

2.2 Boundary conditions and instrumentation

The same concrete mix (described in Section 2.3) and boundary conditions were employed for each test specimen. After filling with concrete, the tubes were welded onto 25 mm thick end-plates, to ensure an even load distribution at each end. The test set-up is illustrated in Fig. 2. Knife-edges were used to allow rotation about the axis of loading eccentricity.

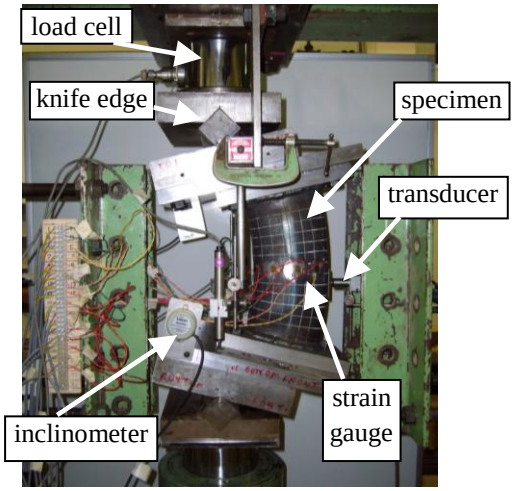

Fig. 2. Test set-up and instrumentation

A compressive load was applied through the knife edges at a steady rate until failure, using a 1000 kN hydraulic actuator. Inclinometers were fixed to the top and bottom of the test specimen to measure the end rotations. The vertical displacement and lateral displacement at mid-height were also measured using linear variable displacement transducers. Strain gauges were employed at eight locations around the specimen circumference, as shown in Fig. 1, to measure longitudinal and circumferential strains.

2.3 Material testing

The concrete mix had an average cylinder strength of 33.9 MPa, which lies within the recommended limits of C20/25 - C50/60 given in CIDECT [13]. The performance of concrete strengths outside of this range has not been as widely documented for concrete-filled tubes. The mix design is given in Table 2, for a maximum coarse aggregate size of 10 mm.

Table 2. Concrete mix design

water	cement	coarse aggregate	fine aggregate
0.56	1	1.72	2.16

The tubular sections had a nominal yield stress of 355 N/mm^2 but tensile coupon tests were carried out in accordance with BS EN ISO 6892-1 [14], using specimens from each tube to obtain the actual value and stress-strain curve. Average values of yield and ultimate stress obtained from the tests are summarised in Table 3.

Table 3. Tensile coupon test results

Tube thickness	Yield stress	Ultimate stress
(mm)	(N/mm^2)	(N/mm^2)
5.0	371	503
6.3	409	529

2.4 Experimental results

Generally, specimens failed by local buckling of the steel on the compression side. Specimens such as MA100-5 and MI25-5 buckled at the mid-height whereas other specimens such as MA25-5 and MI25-6.3 buckled at a lower location. Examples of these failures are depicted (specimens MI75-5 and MI25-5) in Fig. 3.

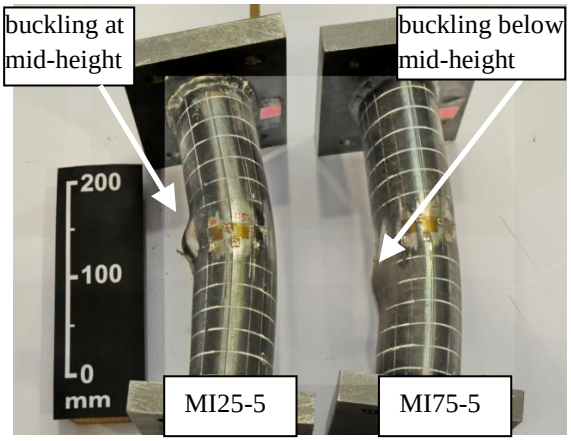

Fig. 3. Failure modes for test specimens MI25-5 and MI75-5.

The bending moment at the mid-height M_{test}, accounting for second order effects, was defined as axial load × (nominal eccentricity + lateral deflection). The maximum loads with corresponding bending moments are shown in Table 4.

Table 4. Maximum axial loads and corresponding bending moments

Specimen ID	$N_{max,test}$	$N_{max,\ test,}/N_{hollow}$*	M_{test}	M_{test}/M_{hollow}*
	kN		kNm	
MA100-6.3	391	1.14	50	1.18
MA25-6.3	851	1.20	23	0.77
MI75-6.3	289	1.17	24	1.22
MI25-6.3	607	1.21	18	1.32
MA100-5	290	1.23	30	1.09
MA25-5	655	1.34	18	0.97
MI75-5	228	1.26	18	1.25
MI25-5	486	1.42	14	1.32

*N_{hollow}, M_{hollow} from [5]

The contribution of the concrete core to the section performance is also presented in Table 4, by comparing the maximum loads and bending moments with those from Gardner et al. [5], in which hollow elliptical columns of the same dimensions as these were subjected to eccentric compression at the same nominal eccentricities. N_{hollow} refers to the maximum axial load on the hollow steel section and M_{hollow} is the corresponding bending moment. The presence of the concrete significantly enhances the axial compressive resistance, providing a greater increase for the 5 mm thick tubes, since these sections have both a lower ratio of steel to concrete in the cross-sectional area and a lower measured yield stress. The maximum axial load also undergoes a greater enhancement for specimens loaded at 25 mm eccentricities than

those at greater eccentricities. An explanation for this is that specimens predominantly loaded in compression achieve a higher confined concrete strength and also experience a lower degree of tensile cracking in the concrete core than those which are mainly subjected to flexure. The enhancement provided by concrete to bending capacity is not as apparent in this comparison. However, since bending moment is related to both the axial load and lateral deformation at the mid-height, and the load increases in all cases, the higher bending moments in the hollow specimens can be accounted for by excessive lateral deformations during buckling. The concrete infill reduces the extent of equivalent lateral deformation in the concrete-filled specimens.

Axial load-displacement relationships are shown in Figs. 4 and 5. For test specimens MA100-6.3 and MA100-5, only a slight decrease occurs in axial load after yield. Specimens MI75-6.3 and MI75-5 yield at significantly lower loads than the major axis bending specimens and undergo a gradual decrease in axial load under increasing axial displacement. Specimens loaded at 25 mm eccentricities exhibit significant decreases in axial load after yield and this is more severe for the 5 mm tubes than the 6.3 mm tubes. In all test specimens except MA100-6.3, the maximum load occurs in the early stages of the test, shortly after yield. The maximum axial force for MA100-6.3 occurs near the end of the test, as the steel tube undergoes post-yield buckling and significant strain hardening.

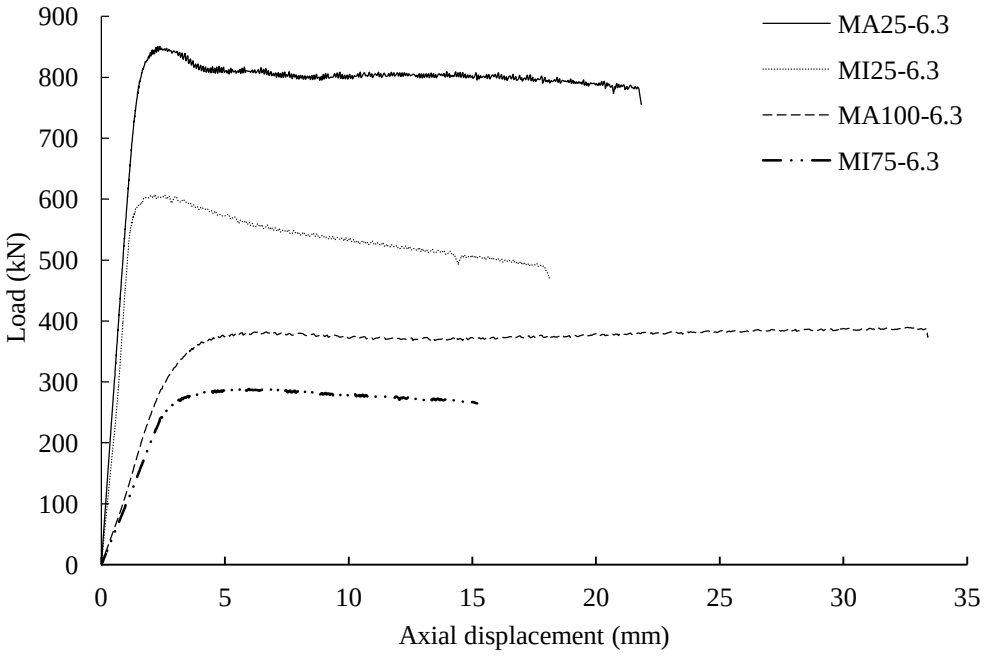

Fig. 4. Load-axial displacement relationships for 6.3 mm EHS.

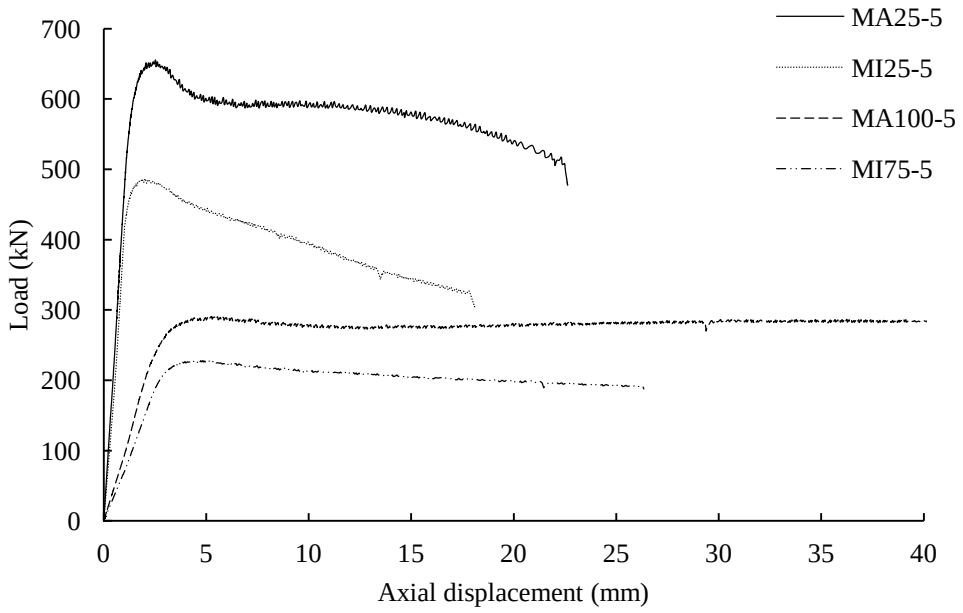

Fig. 5. Load-axial displacement relationships for 5.0 mm EHS.

Moment-rotation relationships for each of the tubes are presented in Figs. 6 and 7 where moment is defined as axial load × (nominal eccentricity + lateral deflection) at mid-height.

There is a noticeable difference between major axis bending and minor axis bending, with the relationship for major axis bending exhibiting a distinct plateau followed by a substantial increase in bending moment in the later stages of the test. For minor-axis bending at an eccentricity of 25 mm, the moment resistance continues to increase after yielding but there is no obvious plateau at yield. For minor axis bending at a 75 mm eccentricity, little increase is observed after yielding, indicating that local buckling of the flat compression face has prevented the attainment of a higher bending moment.

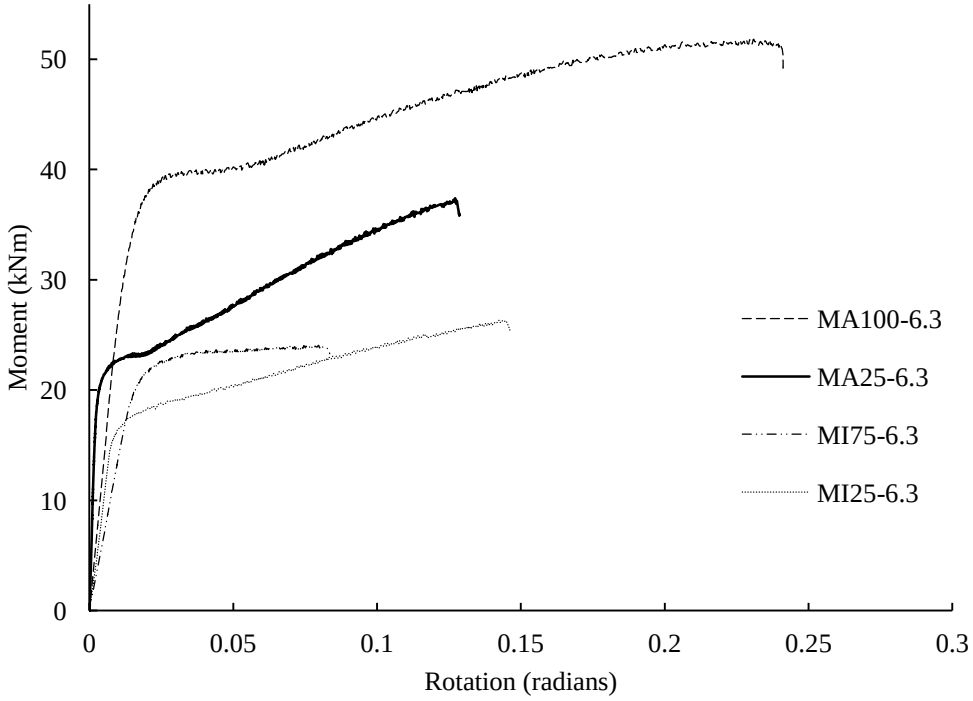

Fig. 6. Moment-curvature relationships for 6.3 mm EHS.

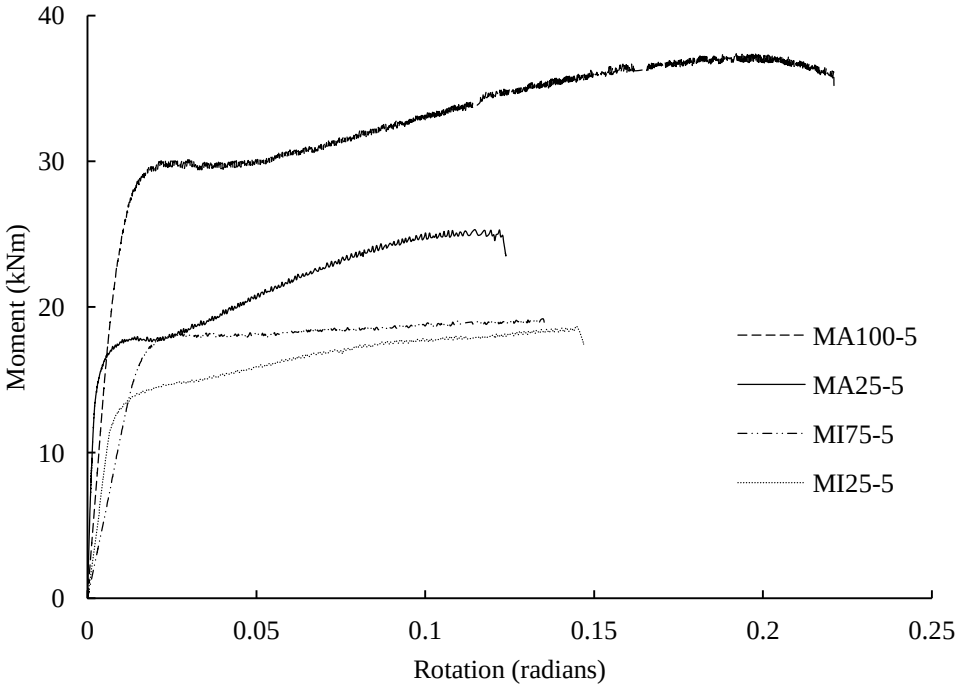

Fig. 7. Moment-curvature relationships for 5.0 mm EHS.

The values and allowable limits of cross-sectional slenderness account for some of the deviations in Figs. 6 and 7 between major and minor axis bending, and the two tube thicknesses. In EN1993-1-1 [15], upper D/t limits of $50\varepsilon^2$, $70\varepsilon^2$ and $90\varepsilon^2$ are used to define Classes 1-3 cross sections respectively for circular hollow sections, where D and t are the diameter and section thickness, $\varepsilon = \sqrt{(235/f_y}$ and f_y is the steel yield stress. The limit of $90\varepsilon^2$ is also adopted in EN1994-1-1 [2] for concrete-filled circular tubes to establish whether or not the effects of local buckling need to be accounted for in cross-section resistance. For application of this recommendation to elliptical hollow sections, Chan and Gardner [4] developed expressions for the equivalent diameter, D_e of the elliptical shape. In contrast to EN1993-1-1 [15] and EN1994-1-1 [2], in which CHS section slenderness limits apply for both compression and bending however, a distinction was made in [4] between compression, major axis bending and minor axis bending, since this affected the point of initiation of local

buckling, from which the equivalent diameter expression was derived. For pure compression and minor axis bending, the equivalent diameter is given by:

$$D_e = 2b^2 / b \quad (1)$$

and for major axis bending, the expression becomes

$$D_e = 2b^2 / a \text{ for } a/b \le 1.357 \quad (2a)$$

$$D_e = 0.8b^2 / b \text{ for } a/b > 1.357 \quad (2b)$$

where a and b refer to the ellipse radii, as shown in Fig. 2. A more detailed expression for D_e in (1) was developed by Ruiz-Teran and Gardner [6] taking account of the tube thickness, and this is presented in Eqs. (3) and (4).

$$\frac{D_{e,EHS}}{2a} = 1 + f\left(\frac{a}{b} - 1\right) < \frac{D_{e,Plate}}{2a} \quad (3)$$

where

$$f = 1 - 2.3\left(\frac{t}{2a}\right)^{0.6} \quad (4)$$

This has been shown to provide more accurate results for sections under pure compression. Following from this analysis, expressions were derived by Gardner et al. [5] for elliptical hollow sections under compression combined with major or minor axis bending. The proposed equivalent diameter used to distinguish between Class 3 and Class 4 sections is given by:

$$D_e = D_{e,b} + D_{e,c} - D_{e,b}\left(\frac{\psi + 1}{2}\right) \quad (5)$$

where $D_{e,c}$ is the equivalent diameter for the case of pure compression calculated using either (1) or (3), $D_{e,b}$ is the equivalent diameter for the case of pure bending, calculated using (1), (2a) or (2b) as appropriate, and ψ is the ratio of maximum tensile stress to compressive stress in the cross-section for a given combination of compression and bending. The D_e/t limit was modified from the value of $90\varepsilon^2$ for compression or bending to $2520\varepsilon^2/(5\psi + 23)$ for compression and bending combined. Following the approach of EN1994-1-1 [2] for concrete-filled circular hollow sections, this hollow section limit is compared with D_e/t ratios where D_e is defined using (5) for each of the test specimens in Table 5.

Table 5. Cross-sectional slenderness limits

Member	D_e/t	$2520\varepsilon^2/(5\psi + 23)$
MA25-6.3	30	62
MA100-6.3	24	72
MI25-6.3	39	65
MI75-6.3	39	73
MA25-5	38	69
MA100-5	30	79
MI25-5	51	72
MI75-5	51	80

All cross-sections used are within the recommended limits from this analysis. Tubes under major axis bending have a significantly lower D_e/t than those under minor axis bending. Owing to the inclusion of ψ in the formulations, specimens loaded under higher eccentricities have a higher allowable cross-sectional slenderness, than those loaded at a 25 mm eccentricity. These observations are reflected in Figs. 4 - 7. Test specimens MI25-5 and MI25-6.3 have the highest D/t ratios relative to the allowable limit for each tube thickness

and these undergo the most severe axial load degradations in Figs. 4 and 5. In contrast, specimens MA100-6.3 and MA100-5, which have the lowest cross-sectional slendernesses in relation to the limit in Table 5, maintain a high axial load with increasing displacement (Figs. 4 and 5), with the load for MA100-6.3 actually increasing beyond the initial peak at a later stage of the test. Specimens that underwent major-axis bending show a plateau in bending moment at yield, followed by distinct bending moment increases in Figs. 6 and 7, as the steel undergoes strain hardening. This distinct shape is not observed in the moment-rotation curves for specimens under minor-axis bending. Hence the cross-sectional slenderness limits presented in Table 5 are reflected in the test-results, with the stockiest section, MA100-6.3 showing the most endurance as the experiment advanced, undergoing local buckling at a later stage and achieving the greatest degree of strain hardening.

3 Finite element modelling

Following the experiments, finite element modelling was carried out using ABAQUS software [16]. Initially eight models were created to simulate the test conditions and once good agreement was achieved with the experimental results, this enabled further numerical modelling.

3.1 Geometry and boundary conditions

Full 3D models were constructed and the geometry and boundary conditions of tested specimens were identical to the experimental set-up. The steel tube and concrete core were modelled as two separate components, and the interaction between these components was defined using the contact properties. 'Hard' contact was adopted in the normal direction and a Coulomb friction model was used tangentially with a coefficient of friction equal to 0.25. Two 100 mm thick plates were modelled at each end of the specimen to simulate the experimental boundary conditions, and these were constrained to the steel tube using a 'tie'

and had a contact interaction with the concrete core. Axial load was applied eccentrically through these plates under displacement control and a Rik's analysis was used as this could capture the post-buckling behaviour of the specimens.

S4R shell elements were chosen to analyse the steel tube. These are general purpose elements with reduced integration, capable of capturing both thick and thin shell behaviour, and consisting of four nodes, with 6 degrees of freedom per node. C3D8R solid continuum elements were employed for the concrete core. These are eight-noded brick elements, with reduced integration, hourglass control and 3 degrees of freedom per node. Chan and Gardner [4] found $2a/10(a/b)$ (with an upper limit of 20) to be a suitable mesh dimension for the modelling of hollow elliptical tubes with S4R shell elements. Dai and Lam [10], obtained effective results for modelling the concrete core, using C3D8R elements with a mesh size between 10 and 20 mm. Hence, a mesh size of 10 mm was employed for each of the components.

3.2 Material models

The stress-strain behaviour of the steel tube was defined using the test data from the tensile coupon tests. The stress-strain behaviour of the concrete was complicated owing to the variation in confinement from the steel tube under axial compression and bending. Therefore two confinement models were considered for composite stub columns under simultaneous compressive and bending loads, and the stress-strain relationships for these are shown in Fig. 8.

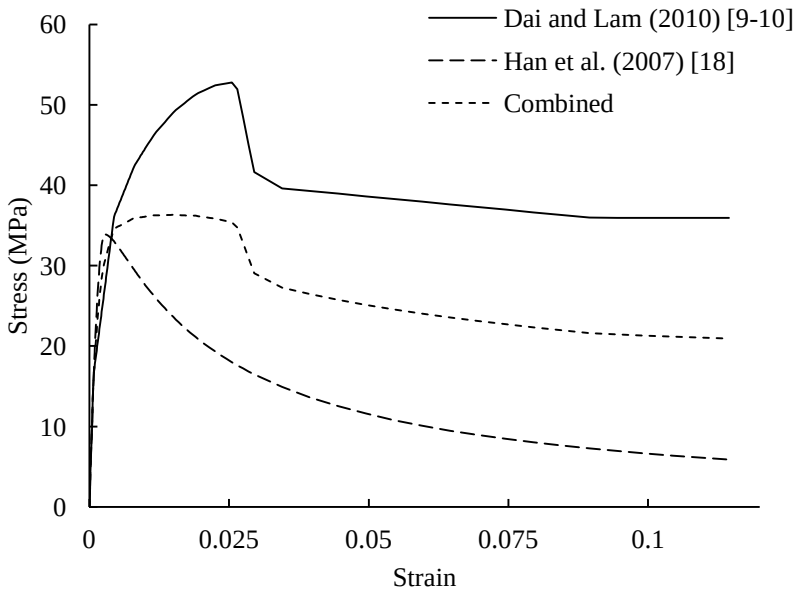

Fig. 8. Proposed stress-strain relationships for confined concrete.

The first confinement model was proposed by Dai and Lam [9 - 10], for elliptical concrete-filled tubes under pure compression, calibrated using data from Yang et al. [7]. The basic equations proposed for the maximum compressive stress, f_{cc} and corresponding strain, ε_{cc} of confined concrete are given by (6) and (7).

$$f_{cc} = f_{ck} + k_1 f_l \tag{6}$$

$$\varepsilon_{cc} = \varepsilon_{ck}\left(1 + k_2 \frac{f_l}{f_{ck}}\right) \tag{7}$$

Eqs. (8) - (9) were justified by Yang et al. [7] and equation (10) was developed by Dai and Lam [10] to account for the elliptical shape.

$$k_1 = 6.770 - 2.645(a/b) \tag{8}$$

$$k_2 = 20.5 \tag{9}$$

$$f_l = f_y \left\{ e^{-1.3\left(\frac{a+b}{t}\right)^{0.34}} \right\} \tag{10}$$

The stress-strain curve for this model is comprised of four parts. The first part assumes linear behaviour up to a stress of $0.5f_{cc}$. This is followed by a non-linear region proposed by Saenz [17] up to the point of maximum stress, where the stress-strain ($f - \varepsilon$) behaviour is described by Eqs. (11) - (14).

$$f = \frac{E_{cc}\varepsilon}{1 + \left(R + R_E - 2\right)\left(\frac{\varepsilon}{\varepsilon_{cc}}\right) - \left(2R - 1\right)\left(\frac{\varepsilon}{\varepsilon_{cc}}\right)^2 + R\left(\frac{\varepsilon}{\varepsilon_{cc}}\right)^3} \tag{11}$$

where $R_E = \dfrac{E_{cc}\varepsilon_{cc}}{f_{cc}}$ (12)

$$R = \frac{R_E\left(R_\sigma - 1\right)}{\left(R_\varepsilon - 1\right)^2} - \frac{1}{R_\varepsilon} \tag{13}$$

and $R_\sigma = R_\varepsilon = 4$ (14)

The third and fourth sections consist of two softening regions, the first extending from (f_{cc}, ε_{cc}) to (f_e, ε_e), and the second from (f_e, ε_e) to (f_u, ε_u), where

$$f_e = \left(\frac{b}{a}\right)^2 \left(\frac{\varepsilon_u - \varepsilon_e}{\varepsilon_u - \varepsilon_{cc}}\right)\left(f_{cc} - f_u\right) + f_u \tag{15}$$

$\varepsilon_e = 10\varepsilon_{ck}$, $\varepsilon_u = 30\varepsilon_{ck}$ and $f_u = k_3 f_{cc}$, with $k_3 = 0.7$ for C30 concrete, 1.0 for C100 concrete and can be obtained using linear interpolation for intermediary concrete strengths.

The second confinement model was proposed by Han et al. [18] for modelling of thin-walled circular and rectangular concrete-filled tubes under pure torsion, following from Han et al.

[19] and Han et al. [20]. For this research, the model for a circular section was employed, and the stress-strain relationship was given by Eqs. (16a), (16b), (17)-(20):

$$y = 2x - x^2 \text{, for } x \le 1 \tag{16a}$$

$$y = \frac{x}{\beta_0 (x-1)^{\eta} + x} \text{, for } x > 1 \tag{16b}$$

$$\varepsilon_0 = \varepsilon_c + 800\xi^{0.2} \text{ x } 10^{-6} \tag{17}$$

$$\varepsilon_c = (1300 + 12.5\,\sigma_0) \text{ x } 10^{-6} \tag{18}$$

$$\beta_0 = \frac{(\sigma_0)^{0.1}}{1.2\sqrt{1+\xi}} \tag{19}$$

$$\xi = \frac{A_s f_y}{A_c f_{ck}} \tag{20}$$

where η = 2 for circular section; $x = \varepsilon/\varepsilon_0$, $y = \sigma/\sigma_0$, and σ_0 is the cylinder compressive strength of concrete.

The elliptical section was attributed with equivalent circular dimensions, following from Equation (2b). The second confinement model produces a significantly lower compressive strength than the first and a more rapid decrease in compressive strength after attainment of the maximum value. From the experimental results outlined in Table 4, it is evident that the confined concrete provides a greater contribution to overall resistance for specimens that are predominantly loaded in compression in comparison with those in bending. In addition to this, there is distinct behaviour between major and minor axis bending, since for the latter, the flatter tube face in compression cannot provide the same degree of lateral pressure as the more curved part in major axis bending. Thus for lower load eccentricities, the Dai and Lam

[10] model was employed, while for higher eccentricities the material model from Han et al. [18] was used, and for intermediate load eccentricities, a 'combined' concrete constitutive model (Fig. 8) was established by linear interpolation between the two models. The proposed limits for implementing the models are given in Tables 6 and 7 for major and minor axis bending respectively, where e' is the loading eccentricity normalised with respect to the cross-section depth in the direction of bending.

Table 6. Proposed concrete constitutive model for major axis bending

Eccentricity range	Concrete model
$e' < 0.50$	Dai and Lam (2010)
$0.50 \le e' < 0.83$	Combined
$e' \ge 0.83$	Han et al. (2007)

Table 7. Proposed concrete constitutive model for minor axis bending

Eccentricity range	Concrete model
$e' < 0.67$	Dai and Lam (2010)
$0.67 \le e' < 1.33$	Combined
$e' \ge 1.33$	Han et al. (2007)

3.3 Results

Good agreement was achieved between the finite element models and experimental results. Failure modes for specimens MI25-5 and MI75-5 are shown in Figs. 9 and 10, from which it can be seen that the FE models have replicated the experimental failure modes. However, it must be pointed out that the failure modes related to the member geometrical shape, material

properties, initial imperfections, etc. These might cause differences between failure modes observed from experiments and predicted by FE modelling.

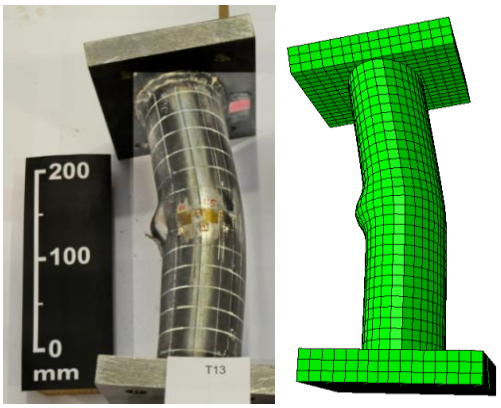

Fig. 9. Comparison of MI25-5 failure modes between experiment and FE modelling.

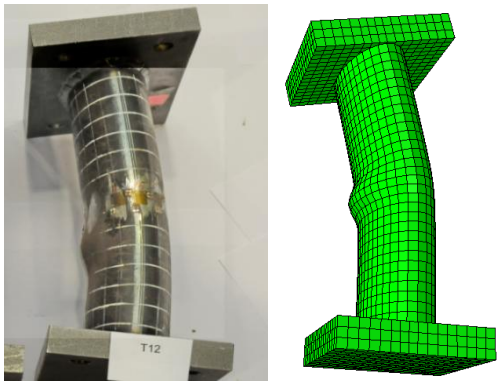

Fig. 10. Comparison of MI75-5 failure modes between experiment and FE modelling.

Comparisons between maximum load and corresponding bending moment for both experimental and finite element models are presented in Table 8. For specimen MA100-6.3, the maximum load in the finite element model occurred in the later stages of the analysis, similar to the experiment. However, for MA100-5, an increase in axial force beyond the initial peak was also observed towards the end of the analysis, which did not arise in the laboratory testing. Hence for consistency, values of $N_{\text{max,FE}}$ and M_{FE} in Table 8 for MA100-5

refer to the initial peak load after yield, which corresponds to the overall maximum force in the corresponding laboratory test. The FE results show a close correlation to the test results, slightly underestimating the load and moment in most cases.

Table 8. Maximum axial load and corresponding bending moment for experiments and FE models

Specimen	$N_{max,FE}/N_{max,test}$	M_{FE}/M_{test}
MA100-6.3	0.97	0.96
MA25-6.3	0.98	1.09
MA100-5	1.00	1.01
MA25-5	1.01	1.07
MI75-6.3	0.98	0.96
MI25-6.3	0.97	0.99
MI75-5	0.97	0.98
MI25-5	0.96	1.04

Load-lateral displacement relationships are illustrated for each tube thickness in Figs. 11 and 12. In most cases the initial stiffness predicted by finite element models was slightly overestimated. This is possibly caused by the difference in initial material properties and initial experimental set-up tolerances between numerical models and physical tests. However, the FE predicted curves that followed a similar shape to the experimental results after yield, and overall the models provided an accurate simulation of the section response.

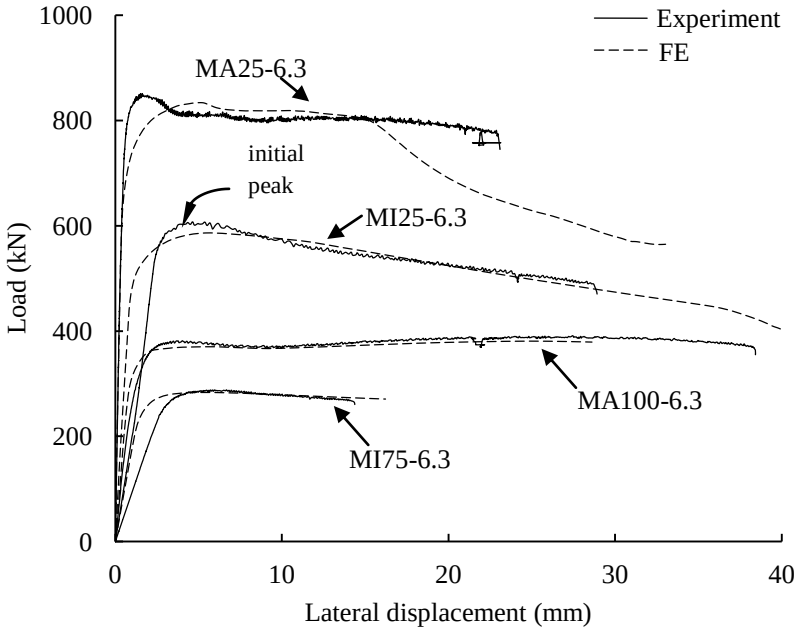

Fig. 11. Load-lateral displacement relationships for 6.3 mm EHS

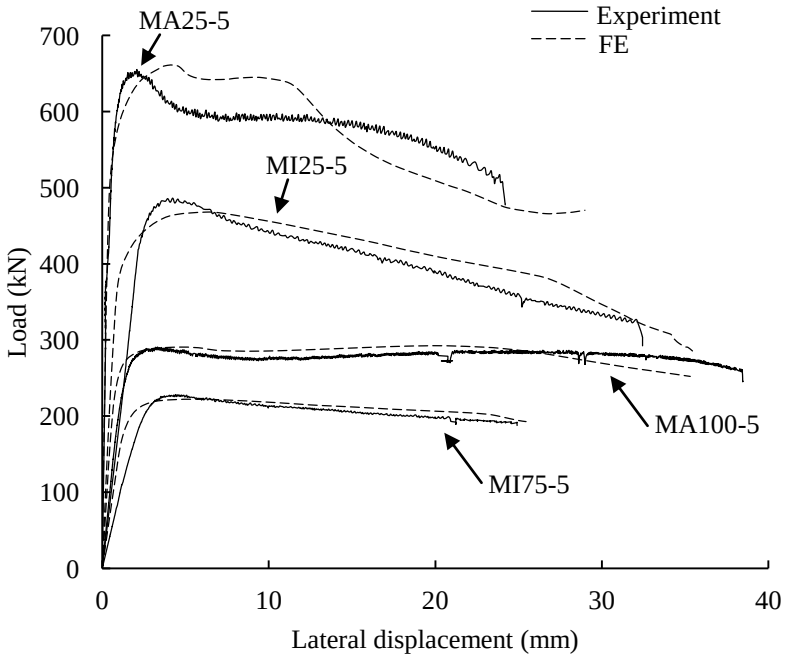

Fig. 12. Load-lateral displacement for 5.0 mm EHS

After satisfactory agreement had been achieved between experimental and numerical results, further finite element models were created, employing eccentricities of 10, 50, 125 and 200

mm about the major axis, and 10, 50 100 and 150 mm about the minor axis. The ultimate axial loads and corresponding bending moments covered a wide range of loading combinations which will be discussed in relation to the interaction curve in Section 4.2.

4 Interaction Curve

4.1 Derivation

Following from the experimental and finite element studies, combined axial force-bending moment interaction curves were derived for the elliptical cross-sections. Generating the exact strain profile of the composite section can be a lengthy and computationally demanding process. The behaviour of the concrete will become plastic while the steel is still elastic or elasto-plastic and the extent of cracking in the core would be difficult to determine. CIDECT [13] recommends assuming plastic stress distributions for the development of combined axial force-bending moment interaction curves, an assumption which is further supported by research such as Roeder et al. [21] for circular concrete-filled tubes.

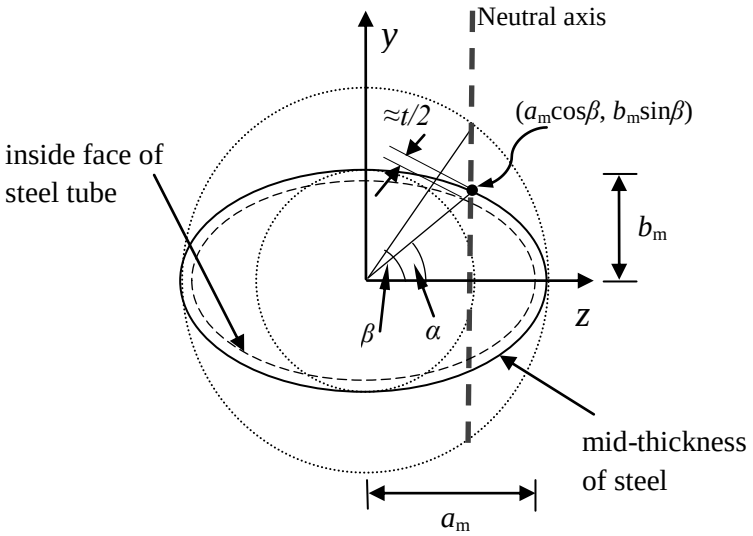

Fig. 13. Geometry for interaction curve derivation

If the wall thickness is assumed to be constant around the perimeter of the ellipse, it is not possible for both the inside and outside faces to satisfy the geometrical equations for this

shape. The profile through the mid-thickness of the steel tube was assumed to be a perfect ellipse and this is presented (outer ellipse) in Fig. 13, where *y* and *z* represent the major and minor axis bending directions respectively, and a_m and b_m denote the maximum and minimum radii. This enables the use of the relationships given by the following equations:

$$\frac{z^2}{a_m^2}+\frac{y^2}{b_m^2}=1 \tag{21}$$

$$z = a_m \cos\beta \tag{22}$$

$$y = b_m \sin\beta \tag{23}$$

Fig. 13 illustrates the section under major axis bending. Since the profile through the centre of the steel tube was assumed to be a perfect ellipse, the shape at the steel-concrete interface deviates from this. For a particular neutral axis location, the distance from the centre of the section to the steel-concrete interface can be estimated by (24), presuming a radial distance of *t*/2 between the two ellipses. The accuracy of this approximation depends upon the angle, α.

$$R_c \approx \sqrt{a_m^2 \cos^2\beta + b_m^2 \sin^2\beta} - \frac{t}{2} \tag{24}$$

Using this distance, the area of concrete in compression and plastic modulus are calculated using (25) and (26):

$$A_{cc} = 2\int_0^{R_c \sin\alpha}\left\{a_m\sqrt{1-\frac{y^2}{b_m^2}}-\frac{t}{2\cos\alpha}\right\}dy - 2R_c^2 \sin\alpha\cos\alpha \tag{25}$$

$$W_{\mathrm{pl,cc}} = 2\int_{0}^{R_c \sin\alpha} \frac{\left(a_{\mathrm{m}}\sqrt{1-\frac{y^2}{b_{\mathrm{m}}^2}} - \frac{t}{2\cos\alpha}\right)^2}{2}\mathrm{d}y - R_{\mathrm{c}}^3 \sin\alpha\cos^2\alpha \tag{26}$$

$$\tan\alpha = (b_{\mathrm{m}}/a_{\mathrm{m}})\tan\beta \tag{27}$$

Taking the steel area as the perimeter through the mean thickness × thickness, the area of steel and plastic modulus are provided by (28) and (29), as used in Chan and Gardner [4].

$$A_{\mathrm{s}} = 2a_{\mathrm{m}}t\int_{0}^{\beta}\sqrt{\sin^2\beta + \frac{b_{\mathrm{m}}^2}{a_{\mathrm{m}}^2}\cos^2\beta}\,\mathrm{d}\beta \tag{28}$$

$$W_{\mathrm{pl}} = 2a_{\mathrm{m}}^2 t\int_{0}^{\beta}\cos\beta\sqrt{\sin^2\beta + \frac{b_{\mathrm{m}}^2}{a_{\mathrm{m}}^2}\cos^2\beta}\,\mathrm{d}\beta \tag{29}$$

The contribution of concrete in tension was ignored in this study, following guidance from CIDECT [13]. Hence the combined axial force-bending moment interaction curve was derived for the cross-section, varying the neutral axis position and using (30) and (31) for each neutral axis position.

$$N = A_{\mathrm{sc}}f_{\mathrm{y}} + A_{\mathrm{cc}}f_{\mathrm{c}} - A_{\mathrm{st}}f_{\mathrm{y}} \tag{30}$$

$$M = W_{\mathrm{pl,sc}}A_{\mathrm{sc}} + W_{\mathrm{pl,st}}A_{\mathrm{st}} + W_{\mathrm{pl,cc}}f_{\mathrm{cc}} \tag{31}$$

Although a factor of 0.85 is applied to concrete stress blocks in other composite cross-section types, EN1994-1-1 [2] recommends exchanging this for a factor of 1.0 for concrete-filled tubes. This may prove to be conservative in comparison with the enhanced confined concrete strength. However, since the full extent of confinement provided by the varying elliptical curvature is unknown, this is a safer estimation than using the full confined strength. Hence a factor of 1.0 was used for the concrete stress-block for both major and minor-axis bending.

For the steel strength, the yield stress from tensile coupon tests was used. Similarly to the concrete strength, this is conservative in some cases, as strain hardening is likely to occur prior to failure.

4.2 Results

The experimental and finite element values of maximum axial load and corresponding bending moment are plotted in Figs. 14-17, for each tube thickness under major and minor axis bending.

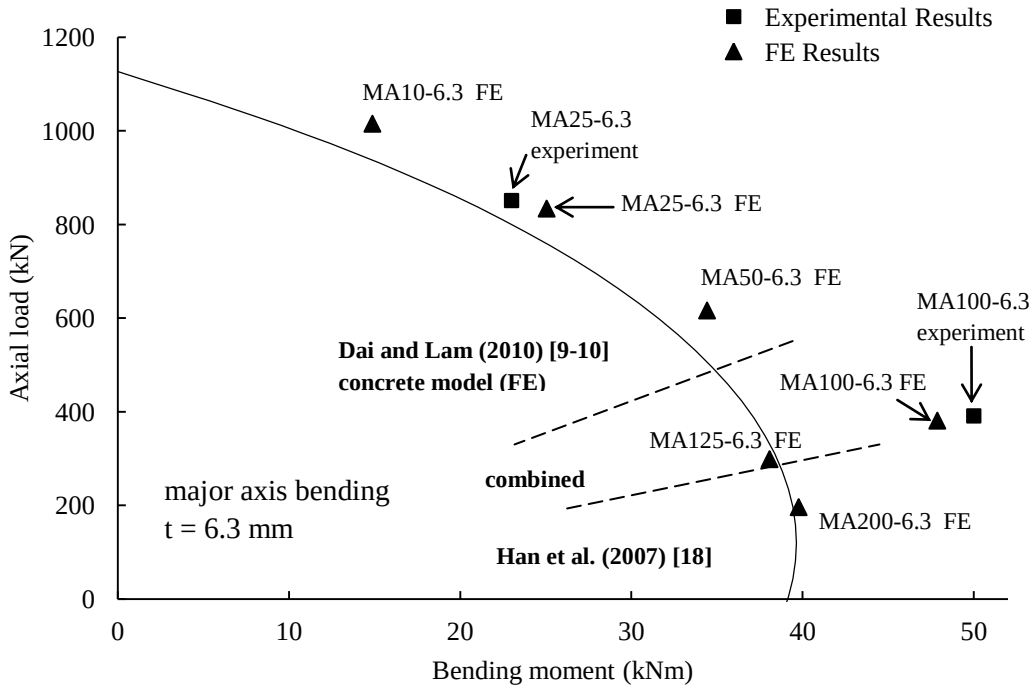

Fig. 14. Combined axial force-major axis bending moment interaction curve for 6.3 mm EHS

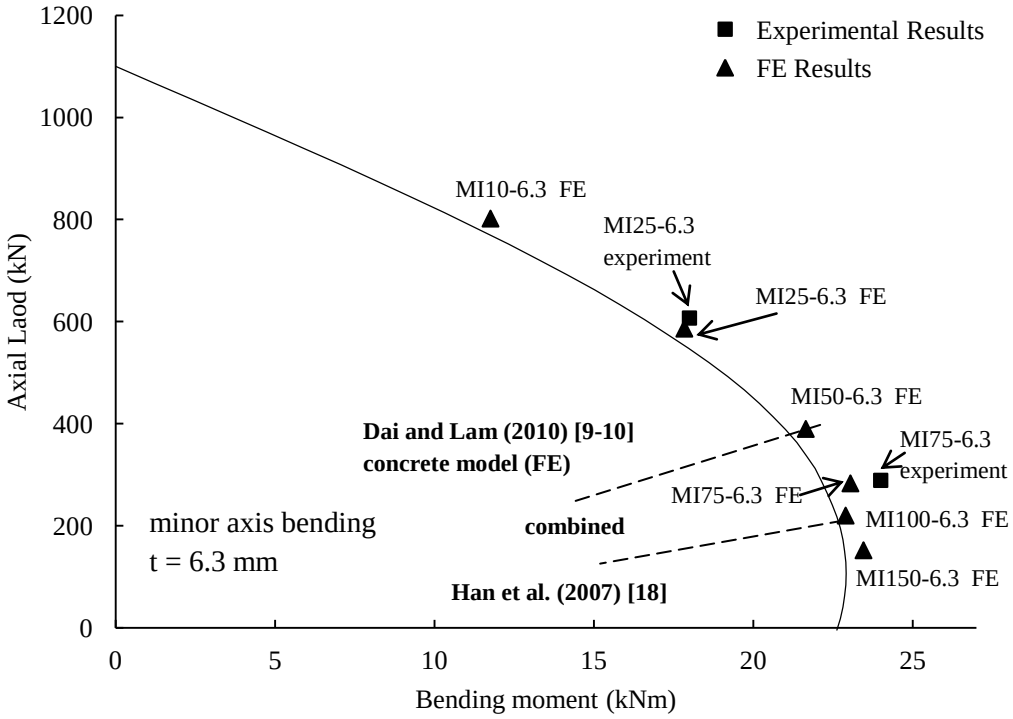

Fig. 15. Combined axial force-minor axis bending moment interaction curve for 6.3 mm EHS

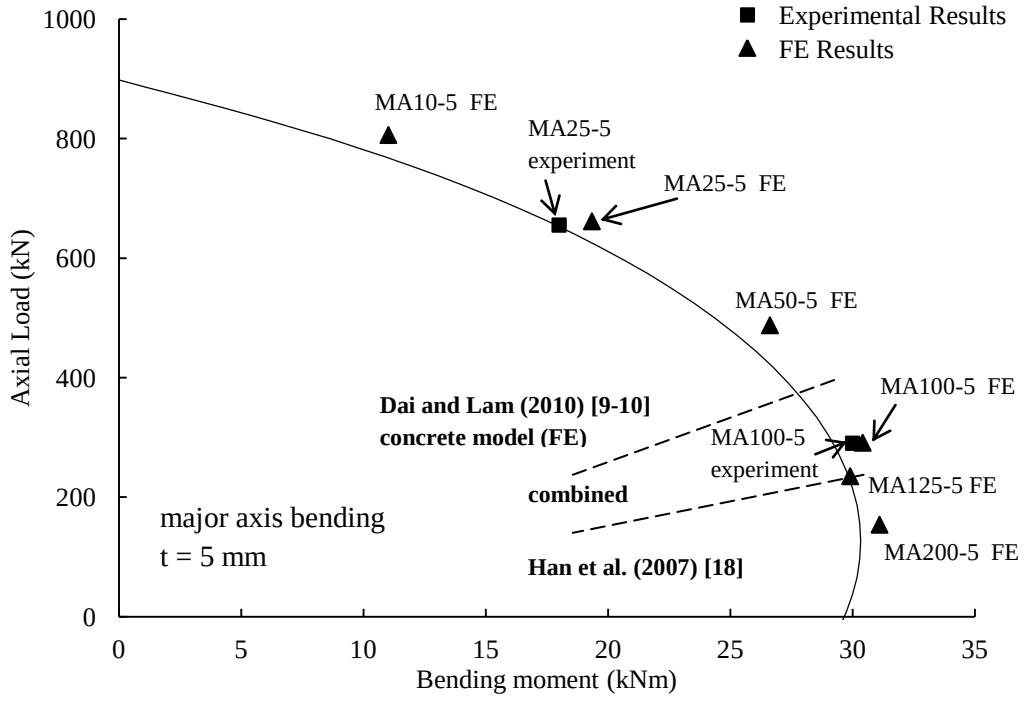

Fig. 16. Combined axial force-major axis bending moment interaction curve for 5.0 mm EHS.

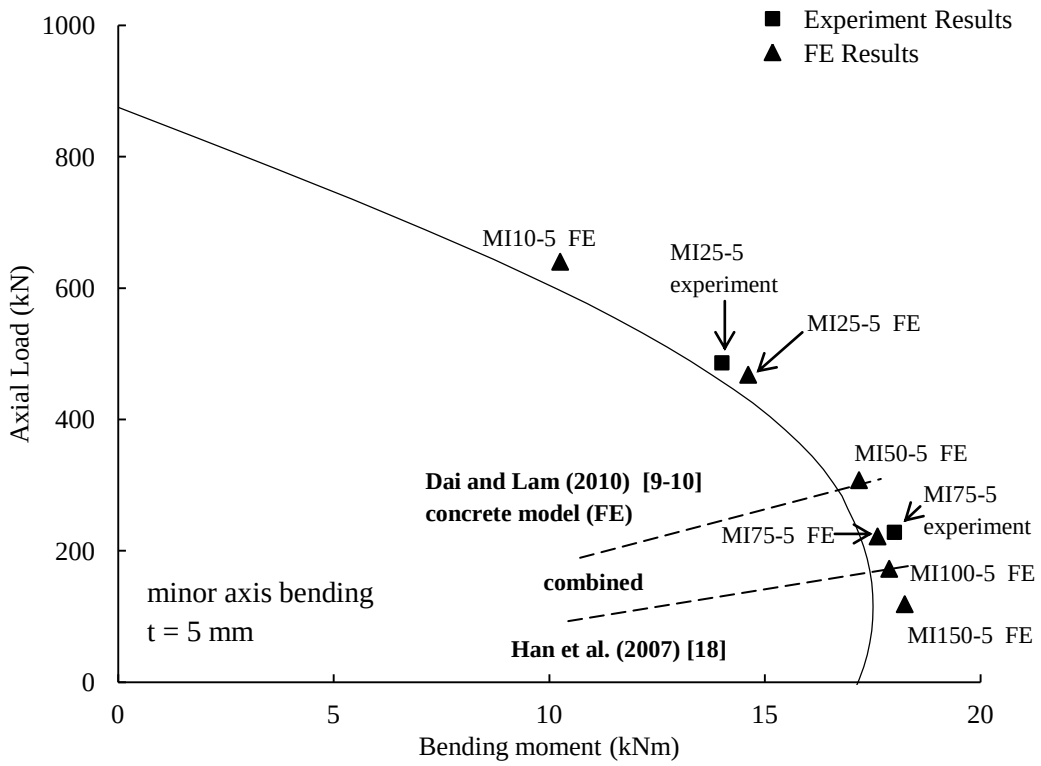

Fig. 17. Combined axial force-minor axis bending moment interaction curve for 5.0 mm EHS

The validity of the interaction curves can be assessed initially using the experimental results. For major axis bending, specimens MA25-5 and MA25-6.3 lie very close to the prediction, while MA100-5 slightly exceeds it. The point for MA100-6.3 has a significantly larger bending moment however, since post-yield buckling occurred, and the steel obtained a higher value of stress than the yield stress employed in the interaction curve generation. In the case of minor axis bending, MI25-5 and MI25-6.3 show very close agreement while MI75-5 and MI75-6.3 achieve marginally higher failure loads. The flatter compression faces for sections under minor-axis bending render them more susceptible to local buckling than sections in major axis bending, and hence these points lie closer to the interaction curve.

The extended finite element model results show close agreement to the interaction curve at all loading eccentricities, confirming the accuracy of the adopted approach. At higher load

eccentricities, using the weaker confinement model from Tables 6 and 7, the curve does not appear conservative in comparison with numerical predictions. Theoretically, sections under this loading condition have a lower cross-sectional slenderness in relation to the allowable limits given by Equation (5) but as discussed in Section 2.4, the concrete contribution to cross-sectional resistance decreases with increasing loading eccentricity, which could limit the resistance at high eccentricities.

5 Conclusions

Experiments have been conducted on concrete-filled elliptical hollow sections under eccentric compression, and the results of these have been successfully simulated using finite element models. Furthermore a combined compression bending-moment interaction curve has been derived for the cross-section, showing good agreement with the experimental and finite element results. From this research, the following conclusions can be drawn:

(1) The response of eccentrically compressed elliptical hollow sections is sensitive to tube thickness, loading eccentricity and axis of bending.

(2) Behaviour of these sections can be successfully captured using full 3D finite element models in ABAQUS. Accuracy is improved through employment of appropriate material constitutive models.

(3) The degree of concrete confinement depends on the eccentricity of applied loading. Specimens which are predominantly loaded in compression provide a greater amount of confinement than specimens which are mostly in bending. Distinct loading eccentricity limits have been proposed for major and minor axis bending in order to define and model the concrete constitutive behaviour.

(4) A suitable interaction curve can be developed by a plastic analysis, as recommended by the CIDECT guidelines [13]. This is efficient for the majority of non-slender

cross-sections, but can be over-conservative for some stocky sections, where the steel can achieve significant strain hardening prior to failure.

Further investigation will be required in the future to examine a wider range of cross-section sizes and slendernesses. For extending this research it would be worth considering alternative methods ([8], [22]) for the interaction curve derivation.

Acknowledgements

The authors wish to thank Tata Steel for supplying the test specimens and Mr. Colin Banks, Mr. Ryan Griffith and Mr. Daniel Hand from the University of Warwick for their work in conducting the experiments. The financial support from the Engineering and Physical Science Research Council (EP/G002126/1) in the UK is also gratefully acknowledged.

References

[1] Susantha KAS, Ge, HB, Usami T. Uniaxial stress-strain relationship of concrete confined by various shaped steel tubes. Eng Struct 2001; 23(10): 1331-47.

[2] BS EN 1994-1-1. Design of composite steel and concrete structures, Part 1-1: General rules and rules for buildings. European Standard, CEN 2004.

[3] Chan TM, Gardner L. Compressive resistance of hot-rolled elliptical hollow sections. Eng Struct 2008; 30(2): 522-32.

[4] Chan TM, Gardner L. Bending strength of hot-rolled elliptical hollow sections. J Constr Steel Res 2008; 64(9): 971-86.

[5] Gardner L, Chan TM, Abela JM. Structural behaviour of elliptical hollow sections under combined compression and uniaxial bending. Adv Steel Constr 2011; 7(1): 86-112.

[6] Ruiz-Teran AM, Gardner L. Elastic buckling of elliptical tubes. Thin-Walled Struct 2008; 46(11): 1304-18.

[7] Yang H, Lam D, Gardner L. Testing and analysis of concrete-filled elliptical hollow sections. Eng Struct 2008; 30(12): 3771-81.

[8] Zhao XL, Packer JA. Tests and design of concrete-filled elliptical hollow section stub columns. Thin-Walled Struct 2009; 47(6-7): 617-28.

[9] Dai X, Lam D. Numerical modelling of the axial compressive behaviour of short concrete-filled elliptical steel columns. J Constr Steel Res 2010; 66(7): 931-42.

[10] Dai X, Lam, D. Axial compressive behaviour of stub concrete-filled columns with elliptical stainless steel hollow sections. Steel Compos Struct 2010; 10(6): 517-39.

[11] Hu HT, Schnobrich WC. Constitutive modelling of concrete by using non-associated plasticity. J Mater Civ Eng 1989; 1(4): 199-216.

[12] Hu HT, Huang CS, Wu MH, Wu YM. Nonlinear analysis of axially loaded concrete-filled tube columns with confinement effect. J Struct Eng 2003; 129(10): 1322-29.

[13] CIDECT Design Guide 5: For concrete-filled hollow section columns under static and seismic loading. International committee for development and study of tubular structures, 1995.

[14] BS EN ISO 6892-1. Metallic materials – Tensile testing – Method of test at room temperature. European Standard, CEN 2009.

[15] BS EN 1993-1-1. Design of steel structures, Part-1-1: General rules and rules for buildings. European Standard, CEN 2005.

[16] ABAQUS, Version 6.11. Dassualt Systemes Simulia Corp., Providence, RI, USA. 2011.

[17] Saenz LP. Discussion of 'Equation for the stress-strain curve of concrete' by P. Desayi and S. Krishnan. J ACI 1964; 61(1): 1229-35.

[18] Han LH, Yao GH, Tao Z. Performance of concrete-filled thin-walled steel tubes under pure torsion. Thin-Walled Struct 2007; 45(1): 24-36.

[19] Han LH, Yao GH, Zhao XL. Tests and calculations for hollow structural steel (HSS) stub columns filled with self-consolidating concrete (SCC). J Constr Steel Res 2005; 61(9): 1241-69.

[20] Han LH, Zhao XL, Tao Z. Tests and mechanics model of concrete-filled SHS stub columns, columns and beam-columns. Steel Compos Struct 2001; 1(1):51-74.

[21] Roeder CW, Lehman DE, Bishop E. Strength and stiffness of circular concrete-filled tubes. J Struct Eng, ASCE 2010; 136(12): 1545-53.

[22] Haque T, Packer JA, Zhao XL. Equivalent RHS Approach for the Design of EHS in Axial Compression or Bending, Adv Struct Eng 2012; 15(1):107-20.